



# Effect of post-heat treatment on residual stress and tensile strength of hybrid additive and subtractive manufacturing

Pengfei Li<sup>1</sup> · Yadong Gong<sup>1</sup> · Chunyou Liang<sup>1</sup> · Yuying Yang<sup>1</sup> · Ming Cai<sup>1</sup>

Received: 4 November 2018 / Accepted: 7 April 2019 / Published online: 24 April 2019  
© Springer-Verlag London Ltd., part of Springer Nature 2019

## Abstract

This paper presents a comprehensive study of the tensile performance, heat treatment, fracture, decrease of residual stress, second-phase particle and microstructures of a 316L stainless steel fabricated by directed laser deposition (DLD) and thermal milling (starting milling temperature at  $250 \pm 50$  °C), a typical hybrid additive and subtractive manufacturing process. Experiments of different post-heat treatment temperatures and tensile tests at room temperature were performed. The residual stress was eliminated with heat treatment at 400 °C for 2 h, and the average residual stress decreased 53.7% while the yield strength and ultimate strength decreased slightly. The fracture surfaces of different heat treatment temperatures were observed. The typical ductile fracture microstructures of dimples were seen in almost all specimens whenever the heat treatment temperature was low or high. The evolution of dimples from formation to destruction by heat treatment was analyzed. The different morphology and composition of the second-phase particles of different heat treatment temperatures were compared. The yield strength of 427.5 MPa, the ultimate strength of 599.27 MPa, and the elongation of 36.48% showed the new hybrid manufacturing technology could be used for further fabrication of components.

**Keywords** Hybrid manufacturing · Thermal milling · Heat treatment · Residual stress · Second-phase particles · Tensile strength

## 1 Introduction

Laser additive manufacturing is one of the new and attractive fabricating technologies [1, 2]. Directed laser deposition (DLD) is one of the most popular technologies [3]. Shorter production cycles result from the application of these technologies, and more complex artifacts can be manufactured without the need of expensive machining and tooling. However, the poor surface quality [4, 5] leads to the emergence of hybrid additive and subtractive manufacturing. In addition, the elimination of residual stress makes heat treatment a hot topic.

With the development of residual stress measurement technology, residual stress analysis has gradually become a necessary means to control and verify product quality in the manufacturing of machinery. The residual stress analysis is also an important method for security inspection for operating equipment. Therefore, residual stress measurement

technology is gaining increasing attention in industry, transportation, military areas, and so on [6–8]. Usually, the residual stress was introduced by rapid heating and cooling during the laser additive manufacturing process, and the high stress zone and low stress zone were interlaced [9]. In order to determine the formation mechanism of residual stress during the DLD of a 316L stainless steel, the Vickers microindentation methods [10], tensile methods, and microstructures [11] were used. Mercelis et al. [12] studied the residual stress of large components produced from 316L stainless steel powder, and they found that the residual stress could be relaxed by a uniform shrinkage and a bending deformation. Pratihari et al. [6] measured the residual stress of the 316L stainless steel by a neutron diffraction method. The characterization of residual stresses of the 316L stainless steel was also studied by Luo et al. [10]. Liu et al. [8] analyzed the distribution of residual stress along the height and horizontal directions. An in-depth measurement of residual stress in the 316L stainless steel was performed by Yadroitsev et al. [13], and they believed that the high thermal gradients resulted in the distribution of residual stress. The surface residual stress measurement method and nondestructive volumetric evaluation method were used to understand the factors influencing residual stress of the 316L

✉ Yadong Gong  
gongyd@mail.neu.edu.cn

<sup>1</sup> School of Mechanical Engineering and Automation, Northeastern University, Shenyang 110819, China

stainless steel [7]. Li et al. [14] compared the residual stresses between DLD surface and hybrid manufacturing surface. He found that the stress was small because of the oxide of the DLD surface, and the stress increased after hybrid manufacturing. Besides that, during the process of fabricating circle, Heigel et al. [15] found the outer was primarily in tension and the inner was in compression; however, the outer after milling machining induced compressive stress.

Heat treatment was used to reduce the residual stress because of the large temperature gradient during the DLD process [16–18]. Post-DLD heat treatment could rectify inhomogeneity in microstructure due to the nonuniform thermal history [19]. Yadollahi et al. [11] investigated the effect of heat treatment on the mechanical and microstructure properties of the direct laser deposition 316L stainless steel. Both Sundararajan et al. [20] and Bandar et al. [21] carried out the experiments of different heat treatment temperatures on 316L, and they found the heat treatment reduced the porosity and improved the plasticity and corrosion resistance. The heat treatment temperatures were 400 °C, 600 °C, 800 °C, 1000 °C, and 1150 °C, which were similar to the [20, 21]. The temperature range included not only low-temperature distressing heat treatment but also overheating at 1150 °C [11]. By choosing suitable heat treatment temperature, the porosity could be reduced and the corrosion resistance could be improved [20]. The maximum residual stress of 316 MPa was reduced to 39 MPa after the post-heat treatment [22]. In addition to the post-heat treatment, the preheating could also effectively reduce the residual stress. Therefore, some scholars carried out experiments with preheating. For example, some substrates were preheated to 120 °C [22] and 80 °C [23]. However, the substrate was preheated by Tang et al. [24] from 1000 to 1100 °C to avoid both the micro-cracks and macro-cracks.

Research to date has focused on the residual stress and post-heat treatment of the DLD process. Hybrid additives and subtractive manufacturing technology have been used to fabricate some components for testing [25, 26]. However, all the milling process were carried out after the DLD part was cooled, which could not freely accomplish the alternation of DLD additive manufacturing and milling subtractive manufacturing. In addition, shrinkage deformation would appear during the cooling process after DLD [27, 28] and lead to the positional deviation in the next DLD machining. Therefore, milling was carried after DLD immediately to reduce the deformation during the cooling, and this work was the basis for processing of complex closed impellers later. Based on hybrid additive and subtractive manufacturing, this paper studied the effect of heat treatment on residual stress and measured the distribution of residual stress of the substrate after DLD. Then, the microstructure, fracture morphology, and fracture mode of different heat treatment temperatures were analyzed. Finally, the yield strength, ultimate tensile strength, and elongation were compared.

## 2 Material and methods

### 2.1 316L stainless steel pre-alloyed powder

In this study, 316L stainless steel powder was used for hybrid additive and subtractive manufacturing. The process parameters have been optimized as follows: the laser power was 1000 W, the vertical floor height was 0.6 mm, the laser scan speed was 480 mm/min, the powder feed rate was 11.28 g/min, and the laser spot diameter is 2.4 mm. The production was performed in a nitrogen gas flow.

Figure 1 shows the powder morphology under a scanning electron microscope (SEM). The spherical particles have a size distribution between 100 and 270 mesh. The nominal chemical composition of the employed 316L stainless steel powder was as follows: Fe—balance, C—0.025%, Si—0.5%, Mn—1.2%, Cr—17%, Ni—13%, Mo—2.5%, S < 0.01%, P < 0.01% (wt%). The chemical composition of the substrate was as follows: Fe—balance, C—0.37–0.45%, Si—0.17–0.37%, Mn—0.5–0.8%, Cr < 0.25%, Ni < 0.25%, Cu < 0.25%, S < 0.035%, P < 0.035% (wt%).

### 2.2 Preheat and post-heat treatment of hybrid manufacturing specimens

Proper preheating can prevent cracks, reduce the residual stress, and improve the metallurgical interaction between the powder materials and substrate [12]. So, high laser power (1800 W) and low powder feed (6.21 g/min) were used to preheat the substrate along the edge of the components before the real DLD process.

The hybrid additive and subtractive manufacturing 316L stainless steel specimens were heated at the different temperatures of 400 °C, 600 °C, 800 °C, 1000 °C, and 1150 °C for 2 h [29], followed by air cooling.

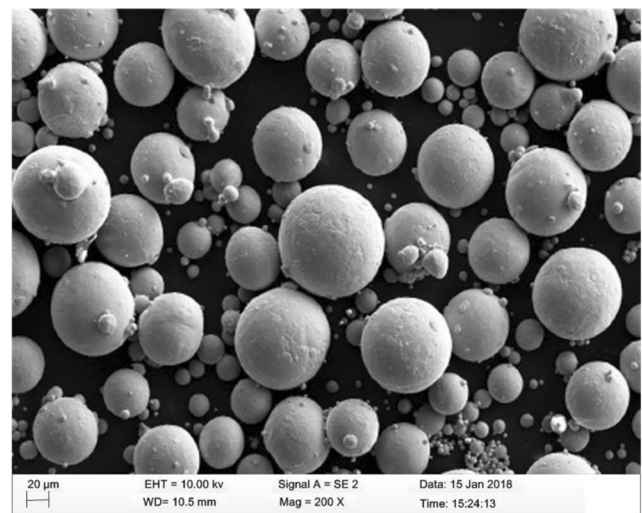
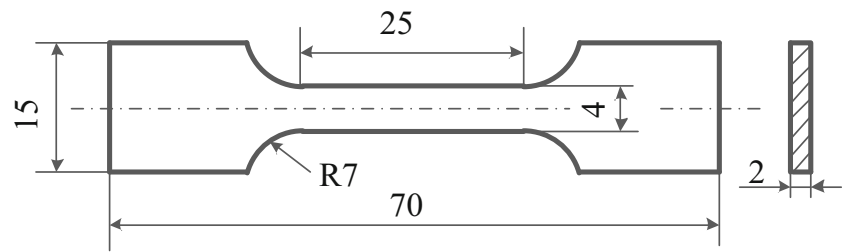


Fig. 1 Characteristic morphology of 316L stainless steel by SEM

**Fig. 2** Geometric sketch of standard tensile plane (mm)



### 2.3 Microstructures and tensile property characterization

The fracture microstructures of the as-built and heat-treated hybrid additive and subtractive manufacturing specimens were characterized using a field emission scanning electron microscope with an acceleration voltage of 15 kV. Before microstructure characterization, the specimens were ground and polished. Aqua regia (vol. 75% HCl, vol. 25% HNO<sub>3</sub>) was used to reveal the general structure of the polished sample.

The tensile strengths before and after the heat treatments were characterized by a high-precision electronic universal testing machine with a constant strain rate of 2 mm/min. The tensile specimen is illustrated in Fig. 2. When the hybrid manufacturing process was finished, the thin plate with good surface quality could be obtained. Then, the tensile specimen would appear by wire electrical-discharge machining. The whole process was shown in Fig. 3.

The hybrid additive and subtractive machining tool is shown in Fig. 4. It can achieve both DLD and milling switching freely. The position accuracy is 8 μm/800 mm,

and the repeatable position accuracy is 5 μm/800 mm. Because of the high process precision, components with high dimensional accuracy can be manufactured. Most importantly, the DLD parts can be milled immediately at a high temperature. By measuring with a laser thermometer, we find that the starting milling temperature is 250 °C ± 50 °C. Therefore, the tensile specimens obtained by DLD and thermal milling can be studied.

### 2.4 Measurement of residual stress

The residual stress of the specimens and substrate were measured by the X-ray diffractometer, which is shown in Fig. 5. The residual stress tester X-350Ac was manufactured by Handan Stress Technologies Co., Ltd., China. The tester meets the standard EN-15305-2008 and the American Standard ASTM E915-2010 standards. Correction with reduced iron powder was required before testing. If the residual stress result was within plus or minus 14 MPa, it was correct. The test result was −9 MPa, so the results showed that it satisfied the stress testing standards, and the device is accurate and reliable [14].

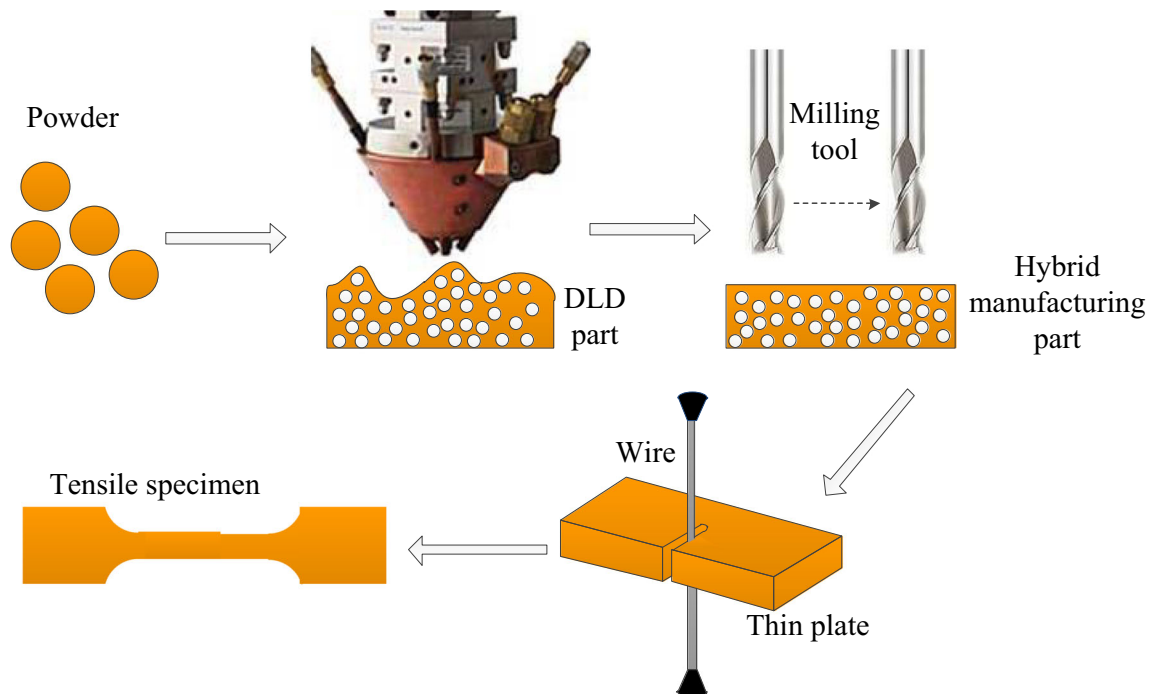
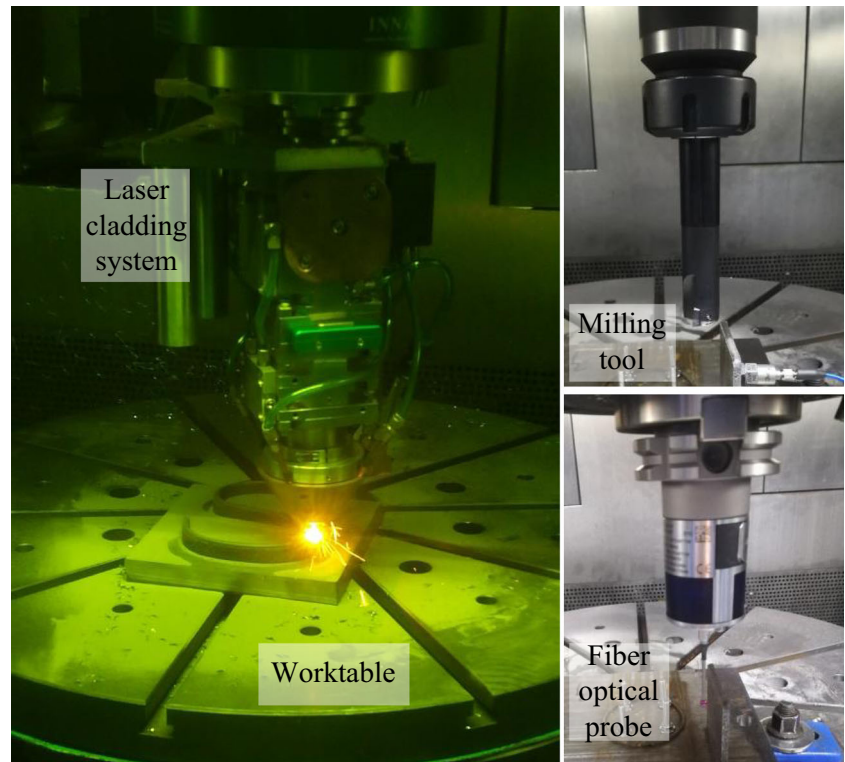


**Fig. 3** Processing of tensile specimen by hybrid manufacturing

**Fig. 4** Hybrid additive and subtractive manufacturing tool



The rolling fixed  $\psi$  method was used to measure the residual stress. The scanning start angle in the  $2\theta$  plane is  $154^\circ$ , the scanning ending angle is  $143^\circ$ , and the scanning step is  $0.1^\circ$ . And the method to determine peak position is the cross-correlation method, with the diffraction crystal plane (311), the high voltage of the X-ray tube at 25 kV, the high current of the X-ray tube at 5 mA, and the counting time of 0.5 s.

The diagram of the roll diffraction method is shown in Fig. 6.  $\psi$  and  $\eta$  are located in two planes perpendicular to each other.

The normal direction of the surface, the normal direction of the diffractive crystal plane, and the direction of the stress to be measured are coplanar. The incident ray, the diffracted ray, and the normal direction of the diffractive crystal plane are in another plane. Based on the measuring principle, the normal direction must be located in the XOZ plane in order to measure the residual stress in the OX direction. Both the incident ray (TO) and the diffracted ray (OC) were at an angle of  $\eta$  with ON. To measure the residual stress at different angles of  $\psi$ , the plane

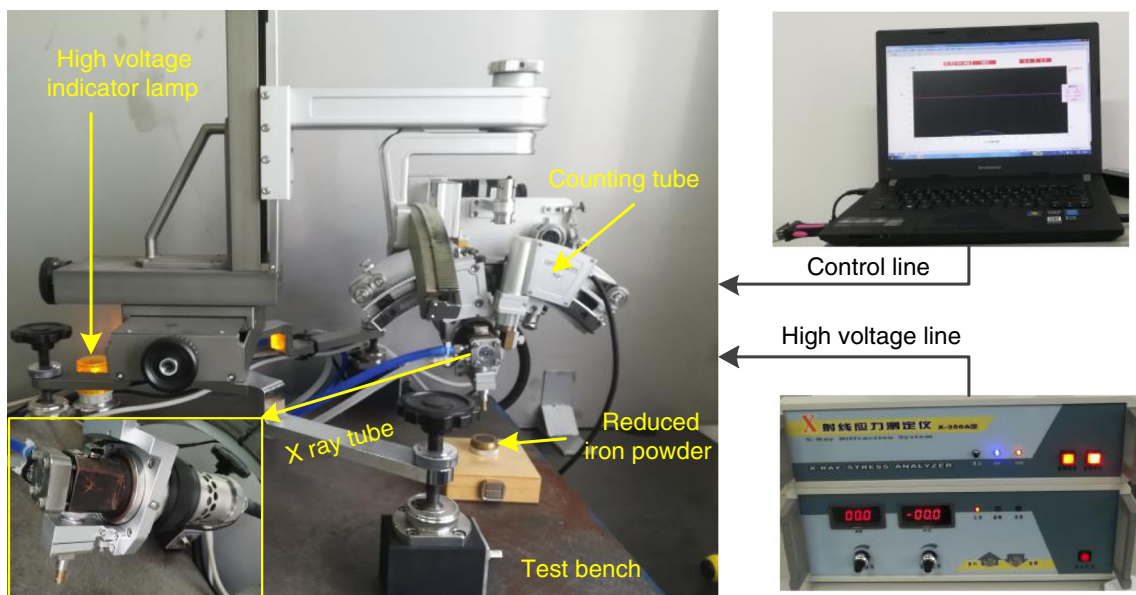


**Fig. 5** Residual stress tester by X-ray diffractometry

$$\sigma_{\theta} = 2K_1\Delta 2\theta$$

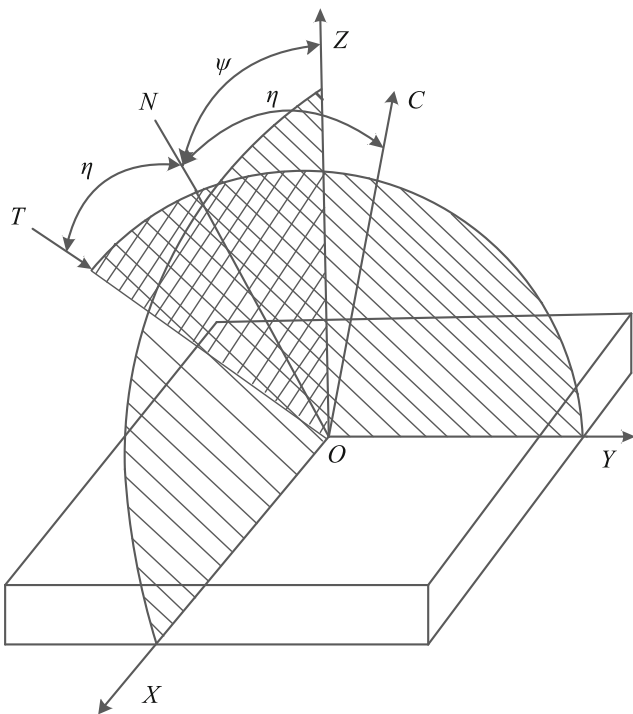
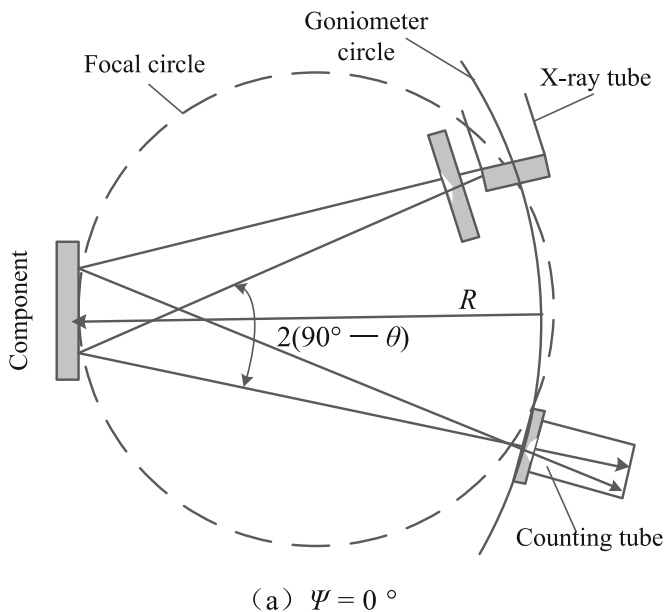


Fig. 6 Geometric schematic of the rolling diffraction method

of TOC should be rotated around the axis of OY. Therefore, the X-ray tube and the counting tube roll simultaneously. The stress calculation formula is shown as:

$$\sigma_{\psi} = K_1 \frac{\partial(2\theta)}{\partial \sin^2 \psi} \quad (1)$$

where  $K_1$  of the austenitic stainless steel is 36.26.



If the  $\psi = 0^\circ$  and  $\psi = 45^\circ$ , it is the fixed  $\psi$  method, and the stress formula is shown as:

$$\sigma_{\theta} = 2K_1\Delta 2\theta \quad (2)$$

According to the design principle of the X-ray polycrystalline diffractometer, the crystal surface was always parallel to the sample surface. Therefore, the normal ( $n$ ) of the sample surface was parallel to the normal ( $N$ ) of the diffraction crystal plane. If the  $\psi = 0^\circ$ , the normal of the sample surface was rotated to the angle of  $\psi$  when the positions of X-ray tube and counting tube were unchanged (Fig. 7a). However, if the counting tube was not on the focal circle, the counting tube must move the distance of  $D$  to detect the diffracted ray. The relationship could be expressed as:

$$R' = R - D = R \frac{\cos[\psi + (90^\circ - \theta)]}{\psi - (90^\circ - \theta)} \quad (3)$$

where  $R'$  is the distance from the counter tube to the surface of the specimen after moving. The residual stress tester used in this experiment has the stress attachment, which can meet the above requirements and calculate the residual stress values.

### 3 Results and discussion

#### 3.1 Residual stress reduction by post-heat treatment at 400 °C

Residual stress often occurs in the process of hot manufacturing of metal materials and their products. And it has a serious impact on the strength, dimensional stability, and service life

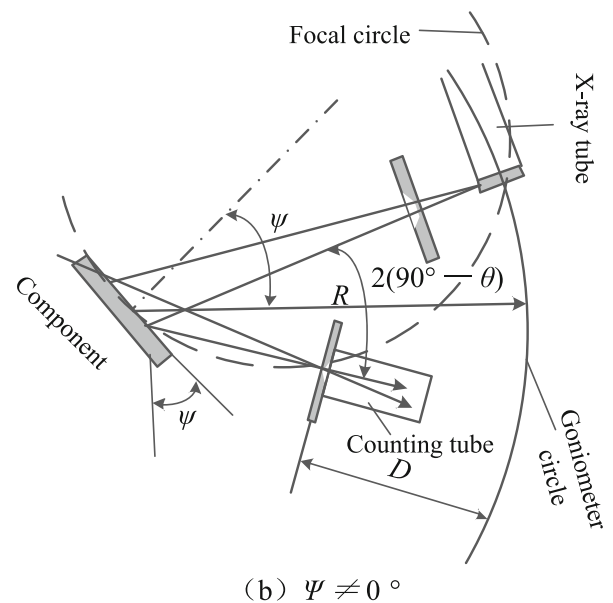
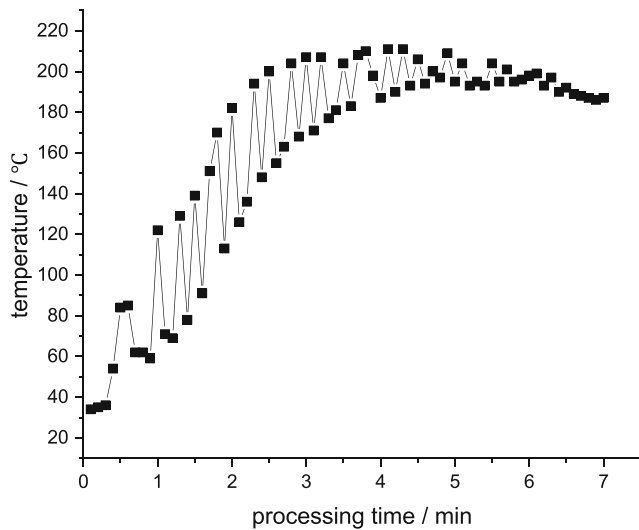


Fig. 7 a, b The focus conditions of  $\psi = 0^\circ$  and  $\psi \neq 0^\circ$



**Fig. 8** In situ measurement temperature of the substrate

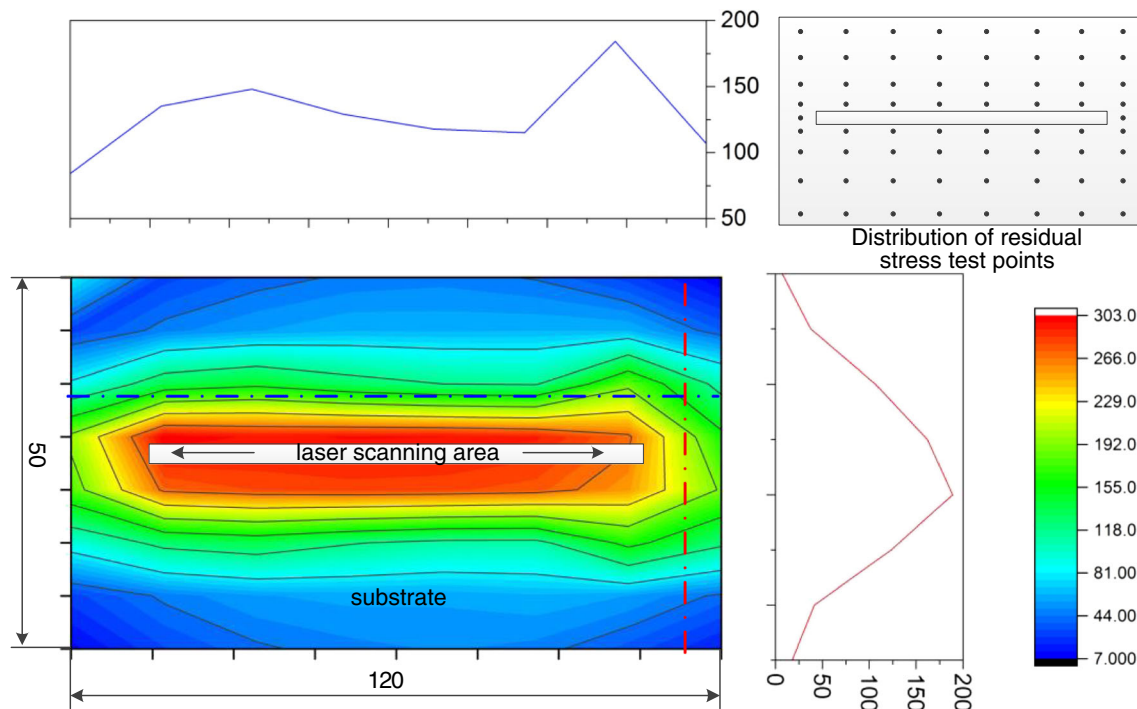
of the product [9]. The stresses distribute not only in the components but also in the substrate. The in situ measurement temperature of the substrate is shown in Fig. 8.

Figure 8 shows that with the increasing of the processing time, the substrate temperature increases rapidly, then stabilizes at approximately 200 °C. The substrate temperature was balanced when the heat input by the laser was almost equal to the heat emitted to the whole environment. The residual stress measurement was carried out when the substrate was cooled. There were 8 channels on the side of the DLD component, and there were 8 test points per channel. The closer to the component, the

denser the test points. The 66 residual stress test points were divided, with the two points on the side of the component. By fitting the measured results in MATLAB, the residual stress distribution map was obtained, as shown in Fig. 9.

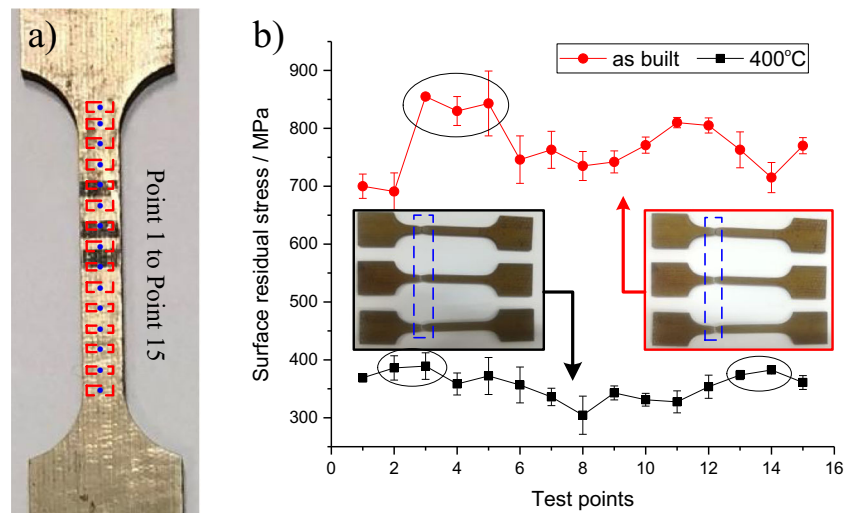
The large residual stress occurred mainly near the laser scanning area, which reached approximately 300 MPa. The stress was reduced with the increasing of the distance between the test point and the laser scanning area, and the stress was the smallest around the corner. The temperature of the laser scanning area was very high, and the temperature gradient was huge. The deformation caused by the temperature was difficult to transfer to the adjacent areas, so there would be large residual stress. In contrast, small stress was observed in the edge region of the substrate because the temperature was lower than in the edge region of the substrate than in the middle area. Another reason for the observation of the small stress was that the deformation could reduce the residual stress. In addition, the residual stress fluctuation was small along the longitudinal direction, and the values at the end were about 100 MPa. The stress value changed greatly in the width direction, and the smallest stress was almost 15 MPa.

Although heat treatment could significantly reduce the residual stress of DLD and milling, excessive temperature would cause serious surface oxidation, which not only affected the residual stress test but also reduced the area of actual load bearing. Therefore, we just compared the residual stresses between the “as-built” hybrid manufactured specimen and 400 °C heat treatment of the hybrid manufactured specimen (as shown in Fig. 10). There were 15 test points distributed in



**Fig. 9** Residual stress distribution map of the substrate after DLD

**Fig. 10** a, b Residual stress comparison of as-built and heat treatment at 400 °C



the working area of the tensile specimen (Fig. 10a), which would reflect the stress of the entire tensile zone. Figure 10 b was the residual stress value before and after heat treatment. The red curve is the residual stress without heat treatment, and the black curve was the residual stress after heat treatment at 400 °C for 2 h and air cooling, and the blue box was the fracture position during the tensile test.

Heat treatment at 400 °C for 2 h would reduce the residual stress of the tensile specimen significantly. The residual stress varied obviously, because the inhomogeneity of the material, inclusions and pores would lead to the milling chatter. After heat treatment, the surface residual stress of the tensile specimen was relatively uniform. The average test residual stress before heat treatment was 769.27 MPa, and it was 356.29 MPa after heat treatment, which indicates that the stress was reduced by 53.7%.

We also analyzed the connection of residual stress distribution and the fracture location and found that all the fracture positions were not in the middle of the tensile specimen. By observing the residual stress values without heat treatment, we found that the third to fifth test points were larger than the others, which was consistent with the location of the fracture. The same rule was found for the specimens with heat treatment. So, it could be concluded that the fracture position of the tensile specimens was near the place where the residual stress was the largest.

Sometimes, the test residual stress was larger than the yield strength of the 316L stainless steel for three reasons: during the milling process, a large blade radius would increase the plastic deformation and surface residual stress of the material but would not affect the internal stress deeper than 140  $\mu\text{m}$  [30]. A super-saturated solid solution would lead to the precipitation hardening and increase the residual stress in the solution heat treatment stage [31]. Deformation during the cooling process would affect the stress because of the high temperature during the laser additive manufacturing process [7, 32].

### 3.2 Effect of different heat treatment temperatures

Based on the hybrid additive and subtractive manufactured specimens, different heat treatment conditions were compared including 400 °C, 600 °C, 800 °C, 1000 °C, and 1150 °C for 2 h with air cooling. Although the heat treatment temperatures were different, there were dimples on the fracture surface observed by the SEM (Fig. 11). And the dimples were the typical microscopic characteristics of ductile fracture [11]. However, different heat treatment temperatures would lead to the different tensile properties. Therefore, we would observe the different macroscopic and microscopic characteristics and analyze the effect on tensile properties.

In order to understand the causes of the fracture, the low magnification of the scanning electron microscope was used to observe the fracture surface. The optical microscope cannot obtain a good image of the uneven fracture because of the small depth of the field. However, SEM could show better image stereoscopic effects and a large depth of field through

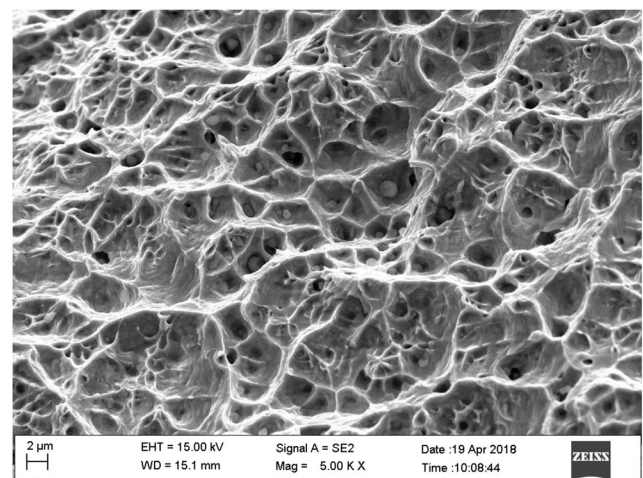


**Fig. 11** Dimples on the fracture surface with SEM ( $\times 5000$ )

secondary electron imaging technology. When the magnification was nearly  $\times 100$ , the fracture morphology obtained is shown in Fig. 12.

Many different factors led to the fracture because inhomogeneity of powder feeding would cause problems such as pores, inclusions, oxidation, and unmelting inside during the DLD process. On the whole, obvious shrinkage can be seen in all specimens when the heat treatment temperature is lower than  $1000\text{ }^{\circ}\text{C}$  (Fig. 12a–d). Ductile fracture of the as-built specimen was the most obvious because there were clear fibrous areas and radiation areas, and the fracture direction could be observed through the stripes in the radiation area (Fig. 12a). When the heat treatment temperature was  $400\text{ }^{\circ}\text{C}$ ,

the internal defects appeared, and there were impurity particles at the edges, which acted as the source of the fracture (Fig. 12b). The fracture surface at  $600\text{ }^{\circ}\text{C}$  (Fig. 12c) and  $800\text{ }^{\circ}\text{C}$  (Fig. 12d) was a small angle, which meant the fracture surface did not correspond to the plane of the maximum normal stress nor correspond to the plane of the maximum shear stress. Therefore, the anisotropy of the material was serious, horizontal performance was poor, and there were plastic inclusions or pores (Fig. 12d). For the 316L austenitic stainless steel, heat treatment at  $1000\text{ }^{\circ}\text{C}$  was high enough to cause the obvious fracture direction and large step defects (Fig. 12e). If the heat treatment temperature increased to  $1150\text{ }^{\circ}\text{C}$ , thermal cracks near the surface would depress the tensile properties (Fig.

**Fig. 12** a–f Fracture morphology of different heat treatment temperatures

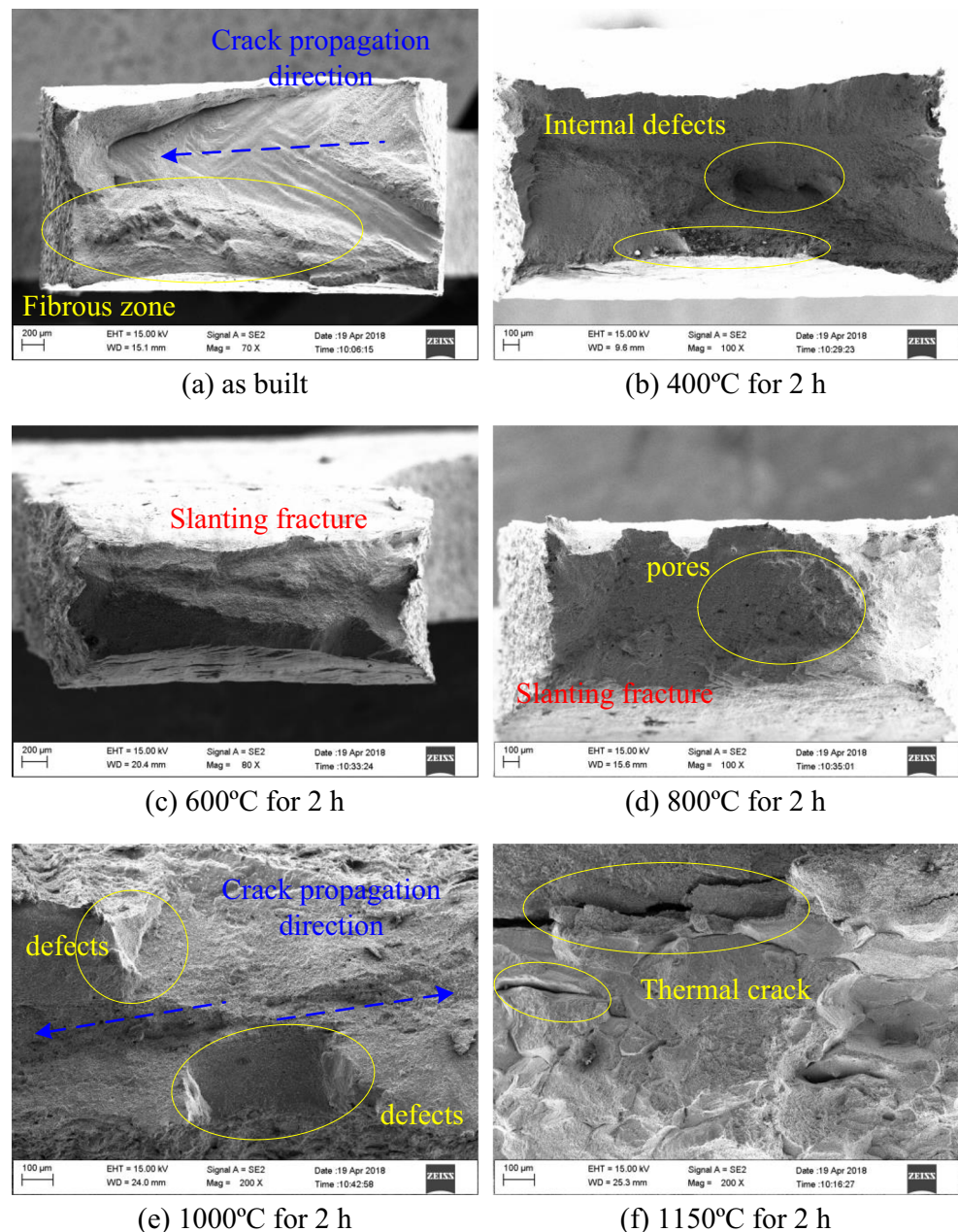
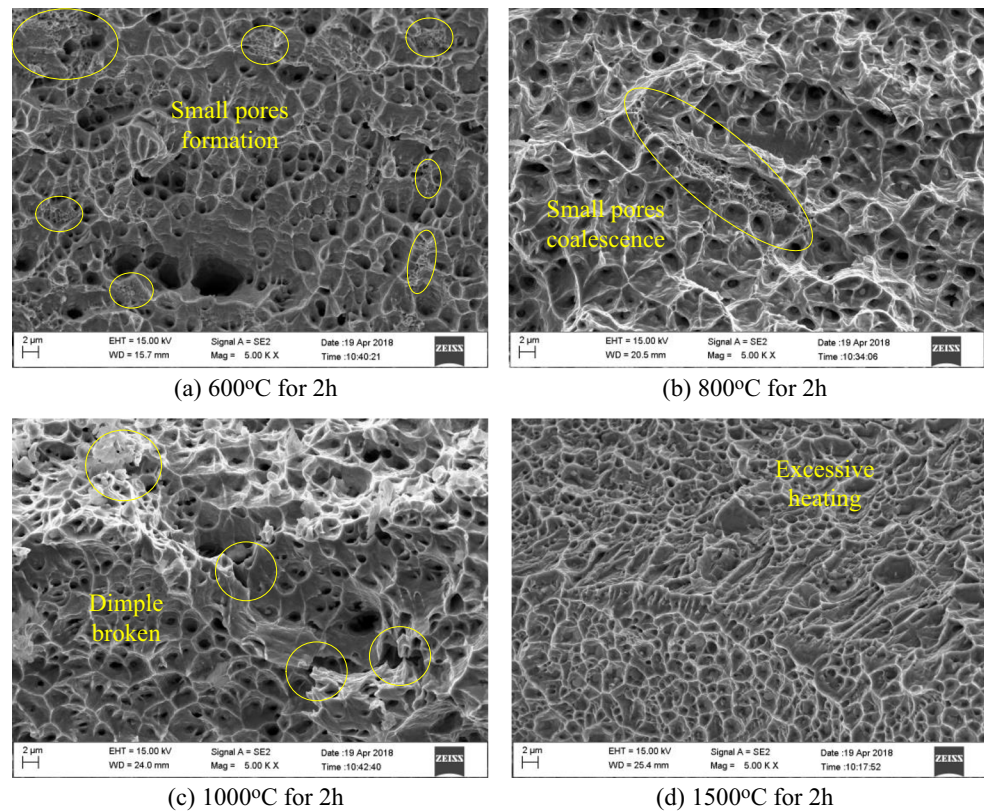




**Fig. 13 a–d** Morphology of dimples at different heat treatment temperatures



12f). The results were like the observations of Yadollahi et al. [11]. In short, the fracture defects were not obvious when the heat treatment was performed at a low temperature. However, the higher the heat treatment temperature, the larger the size of the defects, which would affect the tensile performance under macro-conditions [20].

It was not sufficient to analyze the fracture through the macroscopic analysis. The macroscopic fracture morphology did not fully reveal the microscopic fracture mechanism and other details. And it was needed to analyze the product to determine the cause of the fracture. So, the microscopic fracture was analyzed. The dimples of different heat treatment temperatures are shown in Fig. 13.

Many factors would affect the size of the dimples, such as shape of the second-phase particles, material plasticity, deformation hardening index, stress, and temperature [31]. There were regular dimples on the fracture surface of the as-built specimen with heat treatment at 400 °C (Fig. 11). However, the dimples varied with the heat treatment temperature according to Fig. 13. Smaller and denser dimples gradually appeared around the dimples at the heat treatment temperature of 600 °C (Fig. 13a). When the temperature reached 800 °C, these smaller and denser dimples were connected in a strip (Fig. 13b). When the heat treatment temperature rose to 1000 °C [21], smaller dimples disappeared, and some dimples had broken (Fig. 13c). During the tensile test, the broken dimples were easy to form a fracture source, which might lead to the

fracture and reduce the tensile properties of the specimens. If 1150 °C was used for the heat treatment, excessive heating would lead to the disappearance of the original dimples. Therefore, there were no microscopic characteristics of the ductile fracture, the specimen began to transition from ductile fracture to brittle fracture, and the tensile properties of the specimen were further reduced (Fig. 13d).

By observing the fracture surface of the heat treatment at 1150 °C, we found that the surface was extremely loose, the

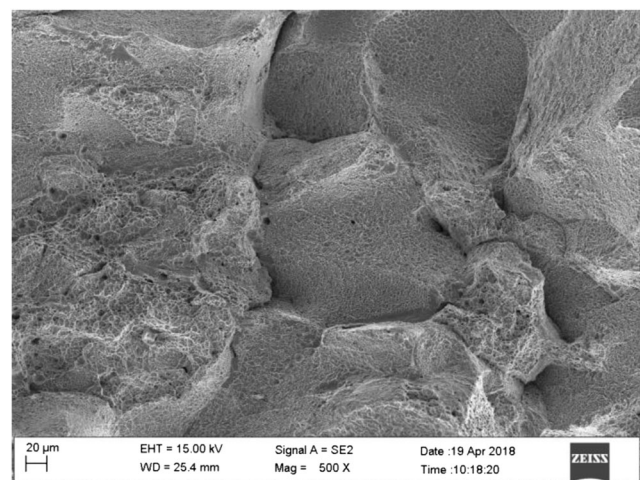


**Fig. 14** Morphology of intergranular ductile fracture with heat treatment at 1150 °C

grain was coarse, and there were small dimples on the grain boundary separation surface (as shown in Fig. 14), which formed the intergranular ductile fracture [21]. On one hand, when the metal was hot-processed or heat-treated, intergranular fracture would appear under stress if the excessive heat caused the partial or overall heating. On the other hand, if the content of the oxygen in the steel exceeded the saturation of ferrite (0.003%), the oxide and oxygen-rich layer formed near the grain boundary would reduce the bonding force of grain atoms and cause the intergranular fracture.

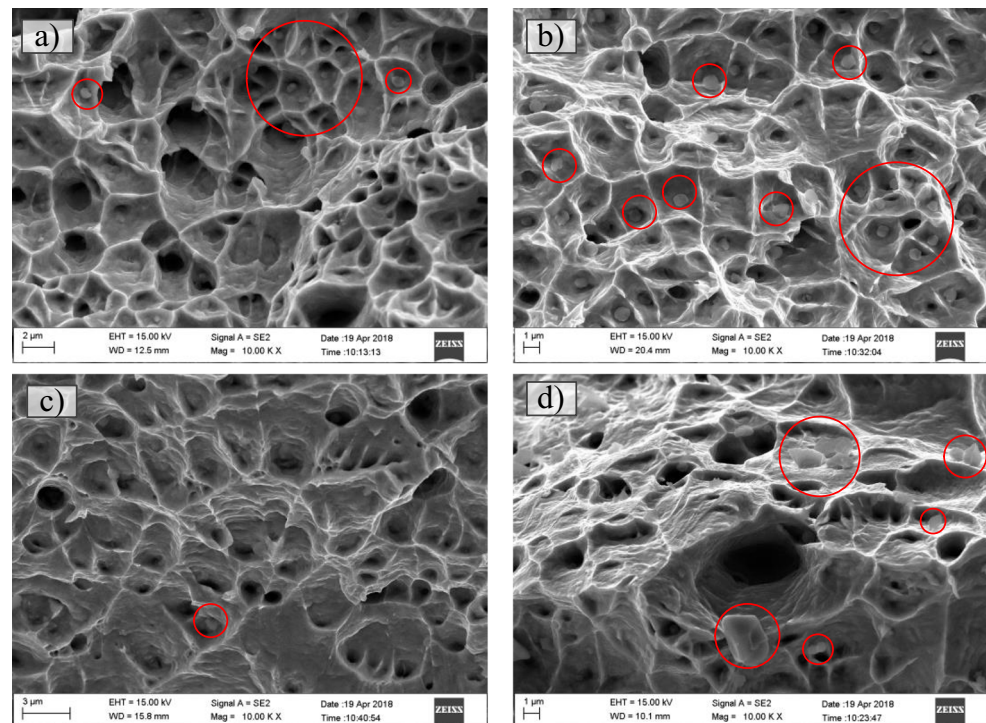
Microstructure of the 316L austenitic stainless steel varied during the process of heating to the austenite range and cooling. Many precipitate phases in the matrix would dissolve during the initial high-temperature austenitization. Then, these elements segregated toward the grain boundary during cooling and precipitated on the grain boundaries. The morphology of the second-phase particles of different heat treatment temperatures is shown in Fig. 15.

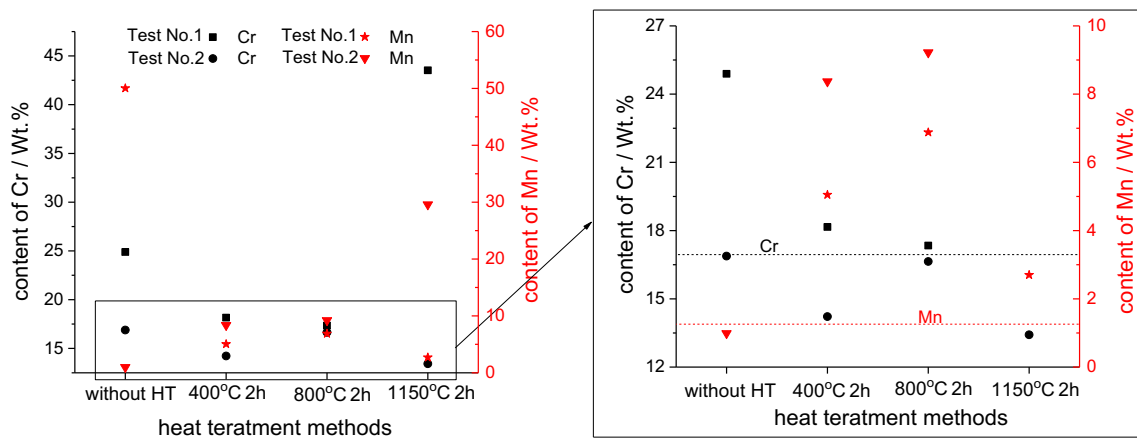
Figure 15 shows that different heat treatment conditions ultimately led to the different second-phase particle morphology. There were many second-phase particles distributed at the dimples with parts of as-built (Fig. 15a) and 400 °C for 2 h + AC (Fig. 15b). However, there were almost no second-phase particles precipitation at 800 °C for 2 h + AC (Fig. 15c). The second-phase particles were flaky, not spherical, when the PHT condition was 1150 °C for 2 h + AC (Fig. 15d). The dimple was a representative microstructure of ductile fractures, and excessive dimples may lead to microscopic cracks and even affect the tensile properties.

The precipitated second-phase particles played an important role in the nucleation, and their size and distribution had a great influence on the size of the dimple. The residual austenite in the 316L stainless steel was ductile phase, which bound strongly to the matrix and improved the ductility and toughness. Besides that, when the crack in the matrix encountered the ductile phase, the ductile phase was prone to initiate plastic deformation rather than brittle fracture, and the plastic deformation consumed a large amount of elastic energy simultaneously. Therefore, the tensile performance of the specimens of the as-built and heat treatment at 400 °C were good. The yield and ultimate strength would show in the next chapter. The tensile strength with heat treatment at 1150 °C was bad, which may be related to the irregular second-phase particles. The plasticity of the flaky second-phase particles was lower than the plasticity of the spherical particles. The nitride in the austenite was sharp-angled. The large stresses and strain at the sharp corners indicated that pores form easily and grow up to reduce the plasticity and toughness [21]. EDS was used to analyze the precipitated second-phase particles (Fig. 16). The main change in elemental content was chromium or manganese, while the other elements hardly changed. Not only that, the degree of oxidation increased with the increase in the heat treatment temperature. Therefore, the precipitated second-phase particles were mainly oxides and nitrides that were chromium-rich or manganese-rich.

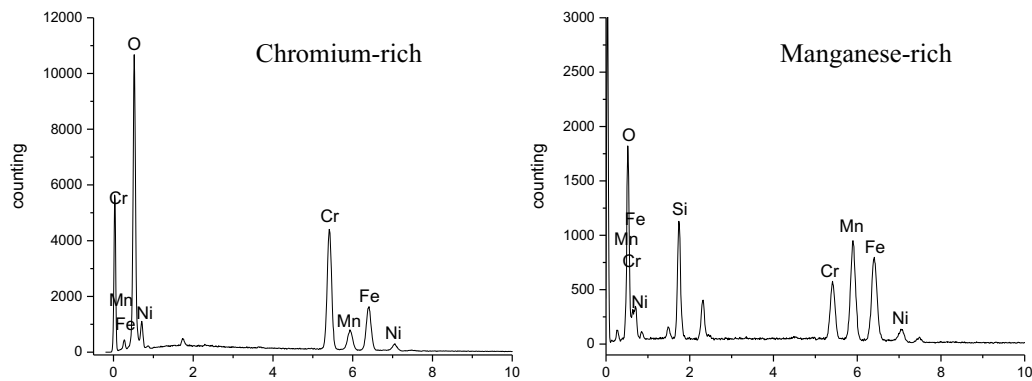
In addition to observing the fracture surface by SEM, the microstructures were analyzed by the optical microscope. The samples were etched by a solution containing HCl (30 ml) and

**Fig. 15** The second-phase particle morphology. **a** As-built; **b** 400 °C for 2 h + AC; **c** 800 °C for 2 h + AC; **d** 1150 °C for 2 h + AC





(a)



(b)

**Fig. 16** Element content analysis. **a** Chromium (Cr) and manganese (Mn) content of precipitated second-phase particles with different PHT conditions. **b** Partial elements of second-phase particles by EDS

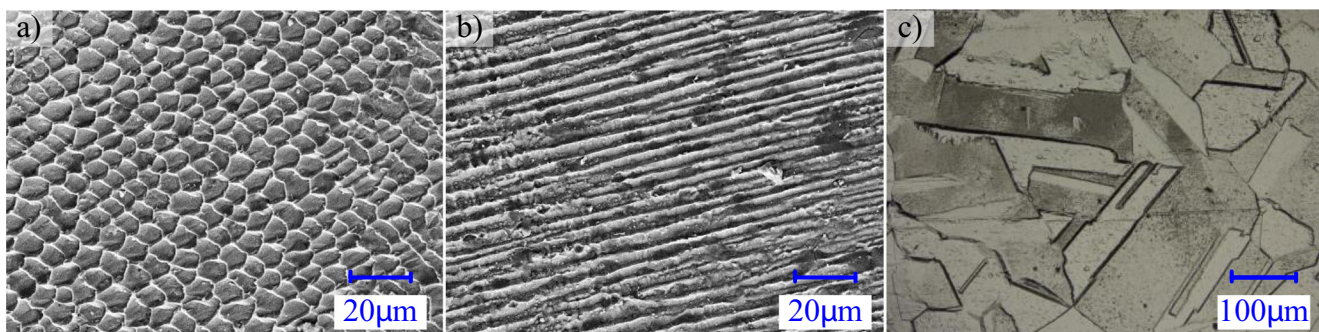
HNO<sub>3</sub> (10 ml) for 60 s. The partial microstructures are shown in Fig. 17.

Figure 17 a shows that it was composed mainly of fine equiaxial crystals when there was no heat treatment. Because the temperature gradients in all directions of the internal workpiece were close to each other. After the low-temperature heat treatment, different temperature gradient caused lots of columnar crystal (Fig. 17b). The equiaxial crystal grew after heat treatment, and the crystal orientation was consistent with the fastest cooling direction of the workpiece

[33]. However, if the heat treatment temperature was too high, the microstructure was a large block, which increased brittleness and led to the decline of the tensile performance [34].

### 3.3 Effect of different heat treatment temperatures on tensile properties

Five different heat treatment conditions were compared (as-built, 400 °C, 600 °C, 800 °C, 1000 °C, and 1150 °C for 2 h with air cooling). The relationship among the yield strength,



**Fig. 17** Microstructure of different PHT conditions. **a** As-built, **b** 400 °C for 2 h + AC, **c** 1150 °C for 2 h + AC

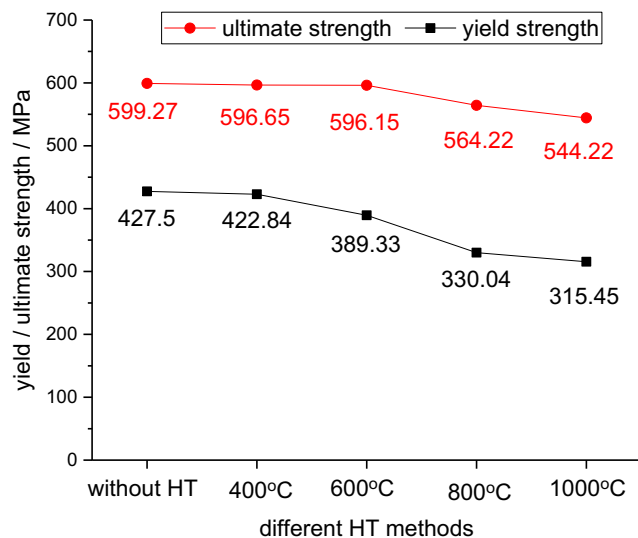


**Fig. 18** Comparison of yield strength and ultimate strength at different PHT conditions

ultimate strength, and heat treatment temperature is shown in Fig. 18. The relationship between the elongation and heat treatment temperature is shown in Fig. 19.

Figure 18 shows that the yield strength and ultimate strength of the specimens decreased with the increasing of the heat treatment temperatures, and the ultimate strength decreased faster than the tensile strength. Because of the high temperature, irregularly shaped second-phase particles would reduce the tensile properties. In addition, broken dimples were more likely to occur, which would indirectly affect the fracture properties and even make the tensile specimens fracture faster (Fig. 13). Both the yield strength and the ultimate strength with the heat treatment at 400 °C did not decrease. And we found that the dimples and the second-phase particles were almost the same by observing Fig. 15 a and b. The tensile

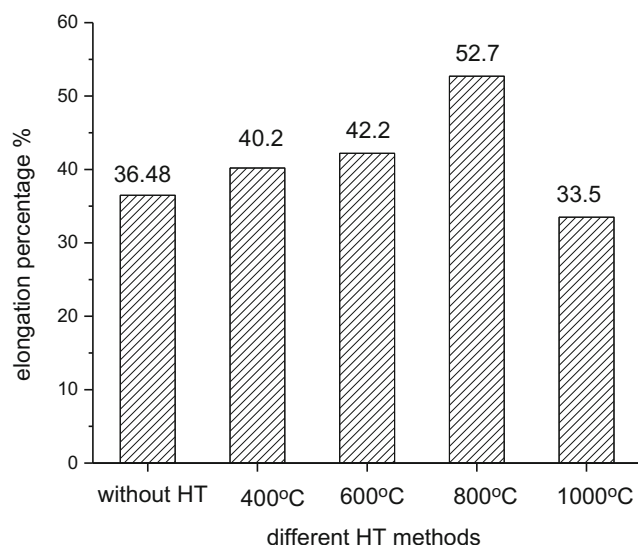


**Fig. 19** Comparison of elongation at different PHT conditions

**Table 1** Yield strength and ultimate tensile strength at the failure of 316 L stainless steel

Condition	YS (MPa)	UTS (MPa)
AM + thermal milling	427	599
AM + thermal milling +400 °C	423	597
AM + cooling milling	459	621
DLD [36]	395	625
DLD [37]	330–345	540–560
SLM as-built [35]	462	565
SLM 650 °C [35]	443	595
SLM As-built [29]	/	600 ± 2
SLM 650 °C [29]	/	618 ± 1

performances gradually decreased with the increase in the heat treatment temperature, which was the same as the results of Fig. 15.

Figure 19 shows that the higher the heat treatment temperature, the greater the elongation if the heat treatment temperature is below 1000 °C. Usually, the high heat treatment temperature softened the material, increased the dimple depth, improved the plasticity of the materials, and then increased the elongation of the tensile specimens. However, excessive heat would make the austenite grains grow up sharply, lead to crystalline fracture, and decrease the elongation if the heat treatment temperature was too high (Fig. 14).

The tensile test results and the literature values for the 316L stainless steel are shown in Table 1 [29, 35–37]. The results from this experiment were as good as the results from the other experiments, which illustrates that the hybrid additive and subtractive manufacturing technology was successful. The average yield strength of as-built was 427.5 MPa, and the average ultimate strength was 599.27 MPa. Although the tensile properties decreased slightly, the residual stress was obviously depressed (Fig. 10). Therefore, the new technology combining the DLD and thermal milling could be used to manufacture some components and simultaneously continue to perform well. Additionally, DLD with thermal milling was comparable to the cooling milling. The average yield strength with cooling milling was 458.9 MPa, and the average ultimate strength was 621.3 MPa. The cooling milling was slightly better than the thermal milling [11]. However, the DLD with thermal milling could avoid the shrinkage deformation when the component was cooling. The aspect of the specific effect of processing parameters on shrinkage deformation will be published in a follow-up study.

## 4 Conclusions

The present article reported on the microstructure, heat treatment, tensile fracture, and properties of directed laser

deposition processing and thermal milling the 316L stainless steel. The main conclusions are summarized as follows.

1. Heat treatment at 400 °C for 2 h would effectively eliminate the residual stress (53.7%). The yield strength and ultimate strength were hardly decreased, and the elongation was simultaneously increased from 36.48 to 40.2%.
2. The dimples and the second-phase particle were varied with the heat treatment temperature. The tiny dimples underwent formation to the junction and then broke with the increase in the heat treatment temperature. If the heat treatment temperature was too high, the microstructure would be too large, crystalline fracture would occur, and the precipitated second-phase particles were irregularly flaky, which would obviously decrease the tensile performances.
3. The yield strength and ultimate strength decreased with the increase in the heat treatment temperature. The ultimate strength was reduced faster than the other. The elongation would be improved when the heat treatment temperature was below 1000 °C.

**Funding information** The authors would like to thank the support of the National Natural Science Foundation of China (No. 51775100), the Fundamental Research Funds for the Central Universities (No. N170306003), and the National Key Research and Development Program of China “Additive Manufacturing and Laser Manufacturing” Key Projects (2017YFB1104202).

## References

1. Gong H, Rafi K, Gu H, Starr T, Stucker B (2014) Analysis of defect generation in Ti-6Al-4V parts made using powder bed fusion additive manufacturing processes. *Addit Manuf* 1:87–98. <https://doi.org/10.1016/j.addma.2014.08.002>
2. Chen Y, Zhang K, Huang J, Hosseini SRE, Li Z (2016) Characterization of heat affected zone liquation cracking in laser additive manufacturing of Inconel 718. *Mater Des* 90:586–594. <https://doi.org/10.1016/j.matdes.2015.10.155>
3. Carroll BE, Palmer TA, Beese AM (2015) Anisotropic tensile behavior of Ti-6Al-4V components fabricated with directed energy deposition additive manufacturing. *Acta Mater* 87:309–320. <https://doi.org/10.1016/j.actamat.2014.12.054>
4. Jackson MA, Van Asten A, Morrow JD, Min S, Pfefferkorn FE (2016) A comparison of energy consumption in wire-based and powder-based additive-subtractive manufacturing. *Procedia Manuf* 5:989–1005. <https://doi.org/10.1016/j.promfg.2016.08.087>
5. Zhu Z, Dhokia V, Nassehi A, Newman ST (2016) Investigation of part distortions as a result of hybrid manufacturing. *Robot Comput Integr Manuf* 37:23–32. <https://doi.org/10.1016/j.rcim.2015.06.001>
6. Pratihari S, Turski M, Edwards L, Bouchard PJ (2009) Neutron diffraction residual stress measurements in a 316L stainless steel bead-on-plate weld specimen. *Int J Press Vessel Pip* 86:13–19. <https://doi.org/10.1016/j.ijpvp.2008.11.010>
7. Wu AS, Brown DW, Kumar M, Gallegos GF, King WE (2014) An experimental investigation into additive manufacturing-induced residual stresses in 316L stainless steel. *Metall Mater Trans A Phys Metall Mater Sci* 45:6260–6270. <https://doi.org/10.1007/s11661-014-2549-x>
8. Liu Y, Yang Y, Wang D (2016) A study on the residual stress during selective laser melting (SLM) of metallic powder. *Int J Adv Manuf Technol* 87:1–10. <https://doi.org/10.1007/s00170-016-8466-y>
9. Liu F, Lin X, Yang G, Song M, Chen J, Huang W (2011) Microstructure and residual stress of laser rapid formed Inconel 718 nickel-base superalloy. *Opt Laser Technol* 43:208–213. <https://doi.org/10.1016/j.optlastec.2010.06.015>
10. Luo KY, Jing X, Sheng J, Sun GF, Yan Z, Lu JZ (2016) Characterization and analyses on micro-hardness, residual stress and microstructure in laser cladding coating of 316L stainless steel subjected to massive LSP treatment. *J Alloys Compd* 673:158–169. <https://doi.org/10.1016/j.jallcom.2016.02.266>
11. Yadollahi A, Shamsaei N, Thompson SM, Seely DW (2015) Effects of process time interval and heat treatment on the mechanical and microstructural properties of direct laser deposited 316L stainless steel. *Mater Sci Eng A* 644:171–183. <https://doi.org/10.1016/j.msea.2015.07.056>
12. Mercelis P, Kruth JP (2006) Residual stresses in selective laser sintering and selective laser melting. *Rapid Prototyp J* 12:254–265. <https://doi.org/10.1108/13552540610707013>
13. Yadroitsev I, Yadroitsava I (2015) Evaluation of residual stress in stainless steel 316L and Ti6Al4V samples produced by selective laser melting. *Virtual Phys Prototyp* 10:67–76. <https://doi.org/10.1080/17452759.2015.1026045>
14. Li P, Gong Y, Wen X, Xin B, Liu Y, Qu S (2018) Surface residual stresses in additive/subtractive manufacturing and electrochemical corrosion. *Int J Adv Manuf Technol* 98:1–11. <https://doi.org/10.1007/s00170-018-2283-4>
15. Heigel JC, Phan TQ, Fox JC, Gnaupel-Herold TH (2018) Experimental investigation of residual stress and its impact on machining in hybrid additive/subtractive manufacturing. *Procedia Manuf* 26:929–940. <https://doi.org/10.1016/j.promfg.2018.07.120>
16. Wauthle R, Vrancken B, Beynaerts B, Jorissen K, Schrooten J, Kruth JP (2015) Effects of build orientation and heat treatment on the microstructure and mechanical properties of selective laser melted Ti6Al4V lattice structures. *Addit Manuf* 5:77–84. <https://doi.org/10.1016/j.addma.2014.12.008>
17. Cain V, Thijs L, Van Humbeeck J, Van Hooreweder B, Knutsen R (2015) Crack propagation and fracture toughness of Ti6Al4V alloy produced by selective laser melting. *Addit Manuf* 5:68–76. <https://doi.org/10.1016/j.addma.2014.12.006>
18. Cheruvathur S, Lass EA, Campbell CE (2016) Additive manufacturing of 17-4 PH stainless steel: post-processing heat treatment to achieve uniform reproducible microstructure. *Jom* 68:930–942. <https://doi.org/10.1007/s11837-015-1754-4>
19. Hunt J, Derguti F, Todd I (2014) Selection of steels suitable for additive layer manufacturing. *Ironmak Steelmak* 41:254–256. <https://doi.org/10.1179/0301923314Z.000000000269>
20. Sundararajan G, Phani PS, Jyothirmayi A, Gundakaram RC (2009) The influence of heat treatment on the microstructural, mechanical and corrosion behaviour of cold sprayed SS 316L coatings. *J Mater Sci* 44:2320–2326. <https://doi.org/10.1007/s10853-008-3200-2>
21. Al-Mangour B, Vo P, Mongrain R, Irissou E, Yue S (2014) Effect of heat treatment on the microstructure and mechanical properties of stainless steel 316L coatings produced by cold spray for biomedical applications. *J Therm Spray Technol* 23:641–652. <https://doi.org/10.1007/s11666-013-0053-2>
22. Cho JR, Lee BY, Moon YH, Van Tyne CJ (2004) Investigation of residual stress and post weld heat treatment of multi-pass welds by finite element method and experiments. *J Mater Process Technol* 155–156: 1690–1695. <https://doi.org/10.1016/j.jmatprotec.2004.04.325>
23. Zhang D, Niu W, Cao X, Liu Z (2015) Effect of standard heat treatment on the microstructure and mechanical properties of selective laser melting manufactured Inconel 718 superalloy. *Mater Sci Eng A* 644:32–40. <https://doi.org/10.1016/j.msea.2015.06.021>

24. Tang HP, Yang GY, Jia WP, He WW, Lu SL, Qian M (2015) Additive manufacturing of a high niobium-containing titanium aluminide alloy by selective electron beam melting. *Mater Sci Eng A* 636:103–107. <https://doi.org/10.1016/j.msea.2015.03.079>
25. Du W, Bai Q, Zhang B (2016) A novel method for additive/subtractive hybrid manufacturing of metallic parts. *Procedia Manuf* 5:1018–1030. <https://doi.org/10.1016/j.promfg.2016.08.067>
26. Flynn JM, Shokrani A, Newman ST, Dhokia V (2016) Hybrid additive and subtractive machine tools - research and industrial developments. *Int J Mach Tools Manuf* 101:79–101. <https://doi.org/10.1016/j.ijmactools.2015.11.007>
27. Withers PJ, Bhadeshia HKDH (2001) Residual stress. Part 2 – Nature and origins. *Mater Sci Technol* 17:366–375. <https://doi.org/10.1179/026708301101510087>
28. Zhang P, Liu Z (2017) Plastic deformation and critical condition for orthogonal machining two-layered materials with laser clad Cr-Ni-based stainless steel onto AISI 1045. *J Clean Prod* 149:1033–1044. <https://doi.org/10.1016/j.jclepro.2017.02.167>
29. Leuders S, Lieneke T, Lammers S, Tröster T, Niendorf T (2014) On the fatigue properties of metals manufactured by selective laser melting - the role of ductility. *J Mater Res* 29:1911–1919. <https://doi.org/10.1557/jmr.2014.157>
30. Nasr MNA, Ng EG, Elbestawi MA (2007) Modelling the effects of tool-edge radius on residual stresses when orthogonal cutting AISI 316L. *Int J Mach Tools Manuf* 47:401–411. <https://doi.org/10.1016/j.ijmactools.2006.03.004>
31. Aboulkhair NT, Maskery I, Tuck C, Ashcroft I, Everitt NM (2016) The microstructure and mechanical properties of selectively laser melted AlSi10Mg: the effect of a conventional T6-like heat treatment. *Mater Sci Eng A* 667:139–146. <https://doi.org/10.1016/j.msea.2016.04.092>
32. Knowles CR, Becker TH, Tait RB (2012) Residual stress measurements and structural integrity implications for selective laser melted Ti-6Al-4V. *Sajie* 23:119–129
33. Thijs L, Verhaeghe F, Craeghs T, Van HJ, Kruth JP (2010) A study of the microstructural evolution during selective laser melting of Ti-6Al-4V. *Acta Mater* 58:3303–3312. <https://doi.org/10.1016/j.actamat.2010.02.004>
34. Chlebus E, Gruber K, Kuźnicka B, Kurzac J, Kurzynowski T (2015) Effect of heat treatment on the microstructure and mechanical properties of Inconel 718 processed by selective laser melting. *Mater Sci Eng A* 639:647–655. <https://doi.org/10.1016/j.msea.2015.05.035>
35. Riemer A, Leuders S, Thöne M, Richard HA, Tröster T, Niendorf T (2014) On the fatigue crack growth behavior in 316L stainless steel manufactured by selective laser melting. *Eng Fract Mech* 120:15–25. <https://doi.org/10.1016/j.engfracmech.2014.03.008>
36. Zheng B, Zhou Y, Smugeresky JE, Schoenung JM, Lavernia EJ (2008) Thermal behavior and microstructure evolution during laser deposition with laser-engineered net shaping: Part II. Experimental investigation and discussion. *Metall Mater Trans A Phys Metall Mater Sci* 39:2237–2245. <https://doi.org/10.1007/s11661-008-9566-6>
37. Vilar R (2014) Laser powder deposition. *Compr Mater Process* 10: 163–216. <https://doi.org/10.1016/B978-0-08-096532-1.01005-0>

**Publisher's note** Springer Nature remains neutral with regard to jurisdictional claims in published maps and institutional affiliations.